Available online at www.sciencedirect.com

jmr&t Journal of Materials Research and Technology

journal homepage: www.elsevier.com/locate/jmrt

Original Article

Interfacial microstructure and strengthening mechanism of dissimilar laser al/steel joint via a porous high entropy alloy coating

Min Zheng [a,b], Jin Yang [a,*], Jiayi Xu [a], Jiawei Jiang [a], Hua Zhang [b,c,**], J.P. Oliveira [d], Xueqi Lv [a], Jing Xue [a], Zhuguo Li [e]

[a] School of Materials Science and Engineering, Shanghai University of Engineering Science, Shanghai 201620, China
[b] School of Advanced Manufacturing, Nanchang University, Nanchang 330031, China
[c] Shanghai Collaborative Innovation Center of Intelligent Manufacturing Robot Technology for Large Components, Shanghai 201620, China
[d] CENIMAT|i3N, Department of Materials Science, School of Science and Technology, NOVA University Lisbon, Caparica, Portugal
[e] Shanghai Key Laboratory of Material Laser Processing and Modification, Shanghai Jiao Tong University, Shanghai 200240, PR China

ARTICLE INFO

Article history:
Received 18 January 2023
Accepted 7 February 2023
Available online 10 February 2023

Keywords:
High entropy alloy
Porous coating
Laser welding
Interfacial microstructure
Mechanical properties

ABSTRACT

A porous high entropy alloy (HEA) coating was prepared on a steel surface by vacuum sintering. The coating was then used as a transition layer during dissimilar laser joining of Al to steel. Compared with the uncoated laser joints, the liquid alloy spread and infiltrated into the porous structure, the contact angle of the weld reduced from 65.8° to 56.7°, and the brazed width increased from 5.1 mm to 5.9 mm, which improved the wettability and spreadability of the molten filler wire on the substrate. In the case of the uncoated steel, the fusion zone/steel interfacial microstructure consisted of laminated $Al_{7.2}Fe_{1.8}Si$ and $Fe(Al,Si)_3$, while it changed to a composite-like structure containing a soft HEA skeleton and hard IMCs which included $Al_{7.2}Fe_{1.8}Si$, Al_3Ni, and $(Al,Si)_2Cr$. In addition, due to the sluggish diffusion effect of HEAs, a layer of gradient nanocrystalline composed of $Al_{7.2}Fe_{1.8}Si$ was generated, which significantly strengthened the dissimilar laser joints with improvements in both the fracture load (~26.5%) and the displacement (~101.8%). The fracture mode changed from brittle to ductile failure when the porous HEA coating was applied, with fracture propagating through the HEA skeleton. This work provides a novel solution for the strengthening of hard-to-join dissimilar combinations.

* Corresponding author.
** Corresponding author.
E-mail addresses: jyang@sues.edu.cn (J. Yang), hzhang@sues.edu.cn (H. Zhang).

https://doi.org/10.1016/j.jmrt.2023.02.040

1. Introduction

As a new class of advanced engineering alloys, high entropy alloys (HEAs) have been extensively studied due to their potential advantages over conventional metallic alloys in terms of strength, hardness, fracture toughness, wear, and corrosion resistance [1], which makes them potential and promising candidates to be used as structural components for diverse engineering applications. Although balancing the trade-off between strength and ductility, and revealing the strengthening and deformation mechanisms are, at the moment, the most studied topics for HEAs [2], their weldability is a key concern before industrial applications using these materials can be considered. Brazing [3], friction stir welding [4], diffusion bonding [5], arc-based welding [6,7], laser welding [8], and electron beam welding [9] have been used for joining similar and dissimilar joints involving HEAs.

Aside from their excellent mechanical performance under wide temperature ranges and environments, HEAs also exhibit four unique characteristics: (i) high entropy effect, (ii) sluggish diffusion, (iii) severe lattice distortion; (iv) and the cocktail effect [10]. By taking advantage of these characteristics, HEAs can also be used as filler materials during the joining of dissimilar materials to suppress the extensive formation of brittle intermetallic compounds (IMCs), thus enabling the increase in both strength, ductility, and toughness of the welded joints [11]. Wang et al. [12] brazed ZrB2–SiC ceramic to Nb using a CoFeNiCrCu HEA filler and the brazed joint was enhanced due to the formation of tooth-shaped Cr_2B and a composite microstructure containing a soft FCC phase and a hard Laves phase. Azhari-Saray et al. [13] comparatively investigated the resistance spot welding of aluminum alloy and low carbon steel with and without an $Al_{0.5}$FeCoCrNi HEA interlayer. Complex IMCs formed at the Al/HEAs interface due to the strong chemical tendency of the HEA constituent elements towards the aluminum alloy, and the pre-existing cracks and hot tearing at the Al-side of the joint were reduced, which were beneficial for the improving the joint tensile shear load.

Table 1 – Chemical compositions of base materials and filler wire (wt.%).

Materials	Cu	Zn	Mg	Si	S	C	Al	Mn	Fe	Co	Cr	Ni
Steel	–	–	–	0.22	0.02	0.18	0.45	0.60	Bal.	–	–	–
5052 Al	0.1	0.1	2.2	0.25	–	–	Bal.	0.1	0.4	–	0.15	–
ER 4047	0.25	0.90	0.08	12	–	–	Bal.	0.045	0.78	–	–	–

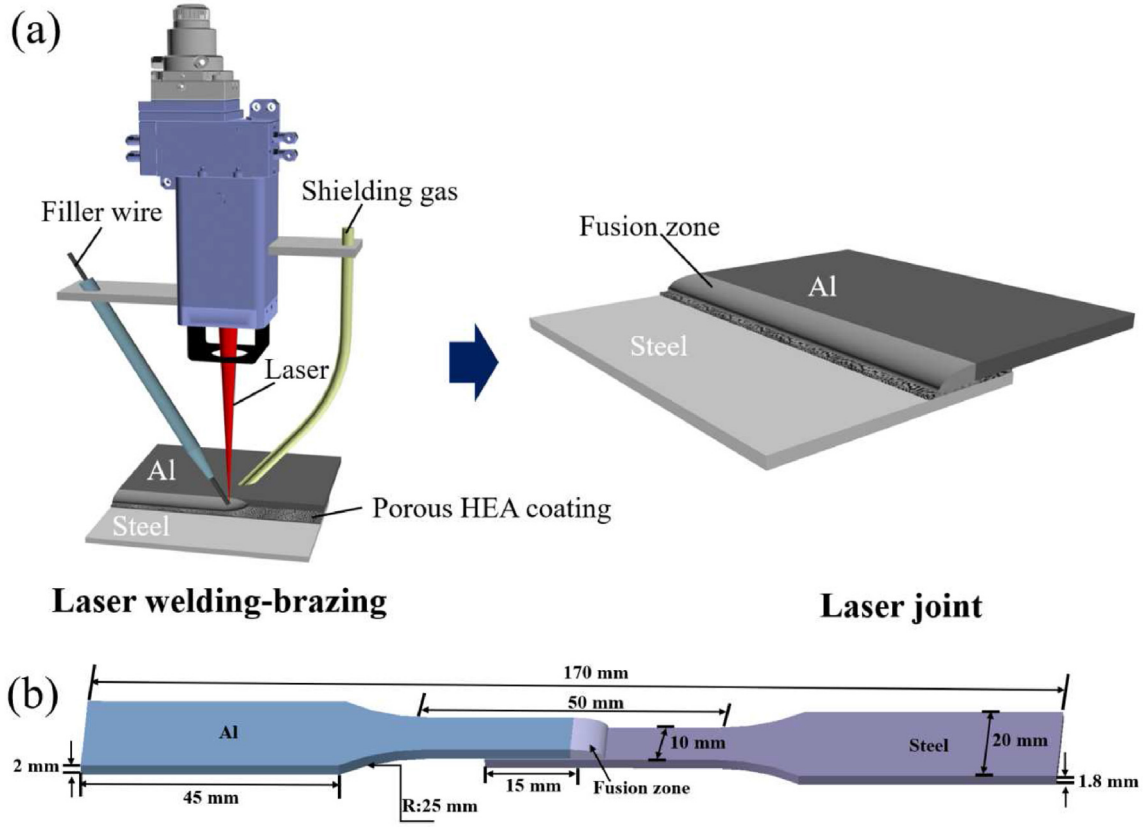

Fig. 1 – (a) Schematic diagram of the laser welding-brazing process of Al to steel via a porous high entropy alloy coating, (b) schematic diagram of tensile sample size.

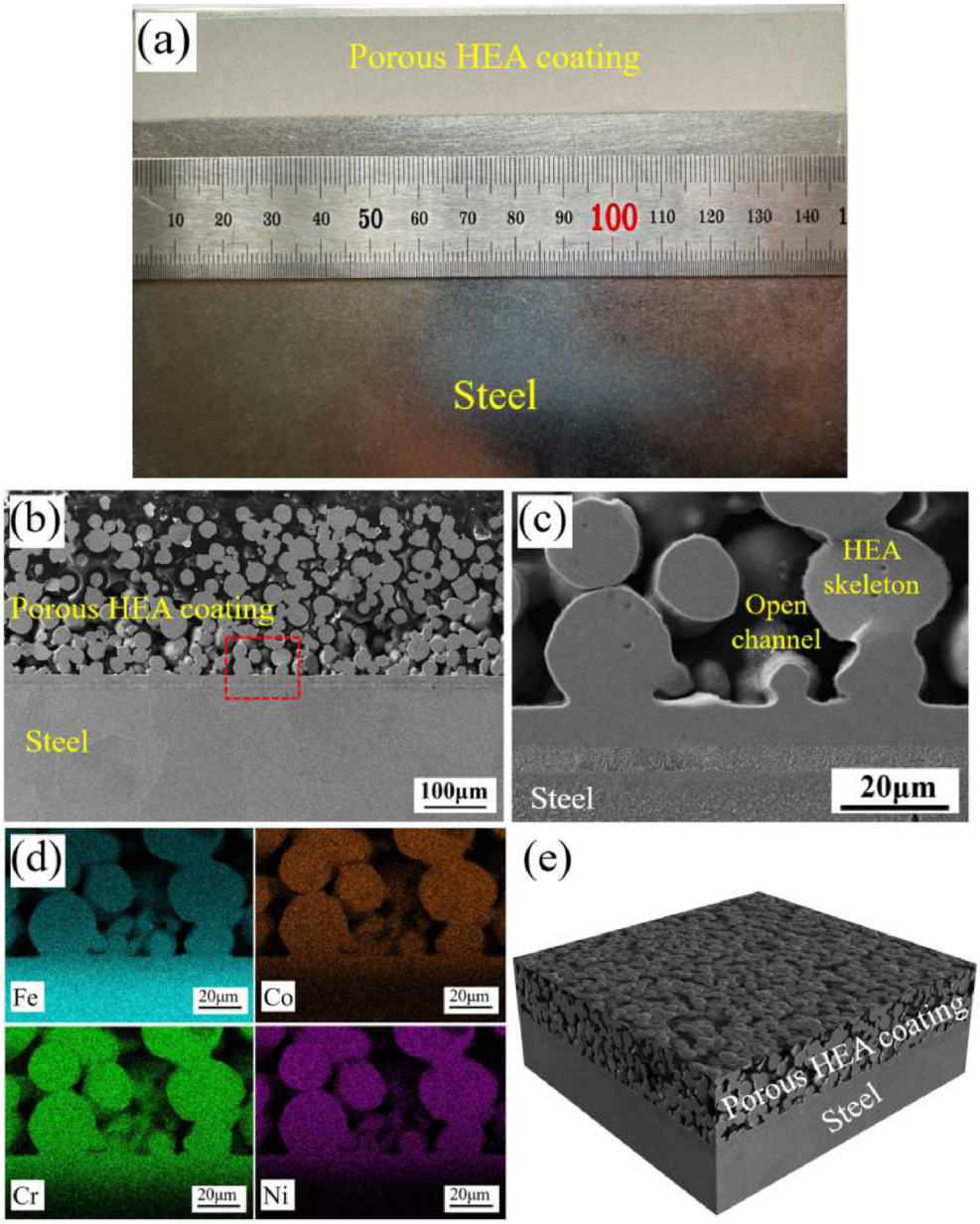

Fig. 2 – (a) Top view appearance of the porous HEA-coated steel, (b) cross-sectional SEM images of the porous HEA-coated steel, (c)SEM image of the red box in (b), (d) EDS mapping in (c), (e) three-dimensional schematic of porous coated steel.

Up to now, the research in this field mainly focuses on the use of HEA as the bulk interlayer or filler metal for the welding of dissimilar materials, while the study on the porous HEA transition layer has been scarcely reported. It is known that porous structures have a unique three-dimensional framework structure with outstanding deformation and absorption capacity, and thus possesses better plasticity and are able to absorb most of the fracture energy [14]. Wang et al. [15] used three-dimensional graphene-reinforced copper foam as an interlayer for vacuum brazing of C/C composites and Nb. The results showed that the addition of a porous interlayer was able to significantly improve the mechanical properties of brazing joints, which was mainly attributed to the good plasticity of the porous interlayer. This was because the porous interlayer absorbed most of the fracture energy and was beneficial to reduce the thermal residual stress during the cooling process. Sun et al. [16] used Ni foam as an interlayer for vacuum brazing of Al_2O_3 ceramics/1Cr18Ni9Ti stainless steel. The results showed that the shear strength of brazed joints increased by 292%, and the thermal residual stress of brazed joints decreased sharply. The above research indicates that the porous layer can effectively alleviate the interface residual stress of dissimilar welded joints caused by the difference in physical and chemical properties as well as metallurgical compatibility, thus improving joint strength.

Laser welding is highly interesting due to its ability to produce a limited extension of both the fusion zone and heat-affected zone (HAZ), with process flexibility and high

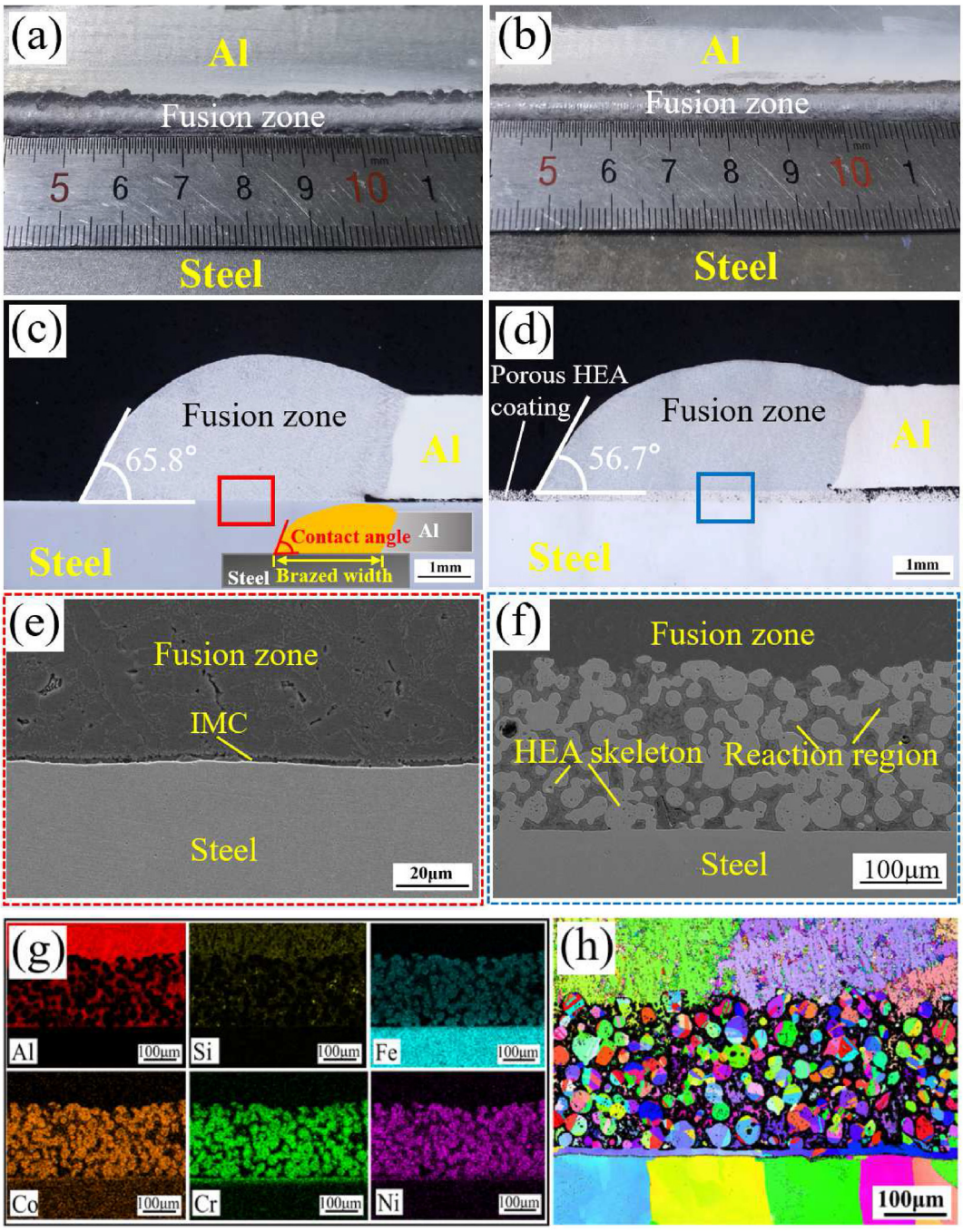

Fig. 3 – (a) Weld appearances of laser Al/uncoated steel joints, (b) weld appearances of laser Al/porous-coated steel joints, (c) cross-sectional of laser Al/uncoated steel joints, (d) cross-sectional of laser Al/porous-coated steel joints, (e) enlarged view at the interface of the red box in (c), (f) enlarged view at the interface of the blue box in (d), (g) EDS mapping in (f), (h) EBSD analysis in (f).

throughput [17,18]. Dissimilar materials laser welding has been extensively conducted [19–27]. However, using porous HEAs transition layer to regulate the interfacial microstructure and improve the laser dissimilar joint as well as the related mechanisms was very rare. To fill this gap, a FeCoCrNi HEA in the form of a porous coating was used as a transition layer in the joining of laser aluminum to steel for the first time. Through a combination of microstructure characterization and mechanical property assessment, a comprehensive understanding of the microstructure evolution and its impact on the use of the porous HEA as a transition layer on the joint properties was obtained.

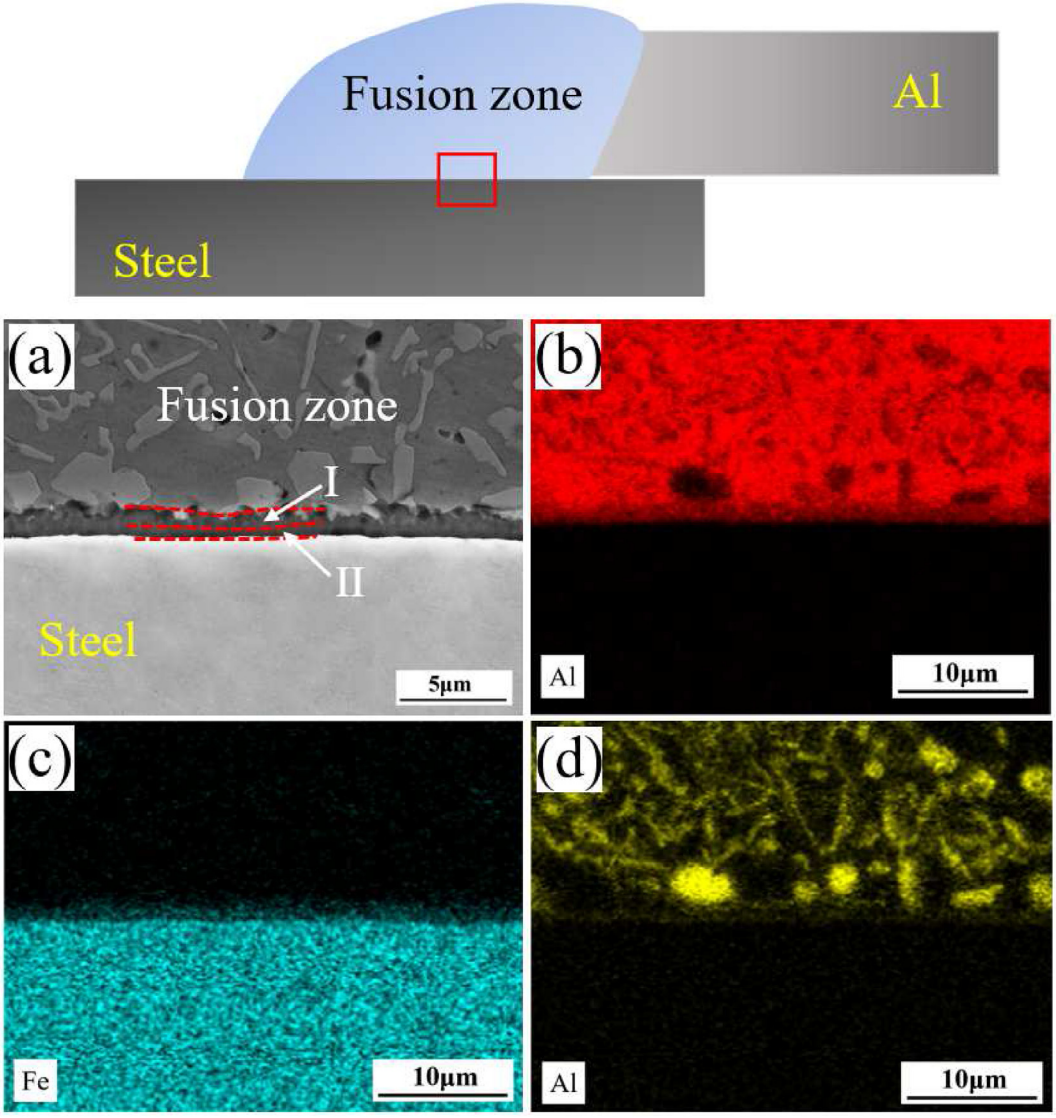

Fig. 4 – SEM image and EDS elemental mapping at the interface of laser Al/uncoated steel joints.

2. Experimental procedures

Low carbon steel and 5052 aluminum alloy, with dimensions of 150 mm × 100mm × 1.8 mm, were selected as base materials. The chemical compositions of the materials are shown in Table 1. A equal atomic FeCoCrNi porous transition layer was pre-coated on the steel surface via furnace sintering. The detailed sintering process was introduced in our previous work [28]. An aluminum-on-steel lap joint configuration with an overlap distance of 15 mm was used, and an IPG YLS-6000 fiber laser was employed for the laser welding-brazing. To mitigate the metallurgical difference between the base materials and the porous HEAs coating, Al–12Si filler alloy was used (Table 1). To minimize the oxidation of the joint, pure argon gas at a flow rate of 15 L/min was used as shielding gas. The experimental layout is detailed in Fig. 1(a). After the optimization of the process parameters, the welding parameters were used as follows: the power of 2300 W, welding

Table 2 – EDS analysis at the points highlighted in Figs. 4 and 5 (at. %).

Region	Al	Si	Fe	Cr	Co	Ni	Possible phase
I	67.39	11.80	20.81	–	–	–	$Al_{7.2}Fe_{1.8}Si$
II	65.23	7.59	27.18	–	–	–	$Fe(Al,Si)_3$
III	67.73	12.23	6.87	10.24	1.61	1.32	$Al_{7.2}Fe_{1.8}Si$
IV	77.78	3.34	4.91	0.37	4.51	9.09	Al_3Ni
V	91.46	7.29	0.27	0.34	0.25	0.39	α-Al+β-Si eutectic
VI	14.07	48.53	2.67	34.13	0.23	0.37	$(Al,Si)_2Cr$

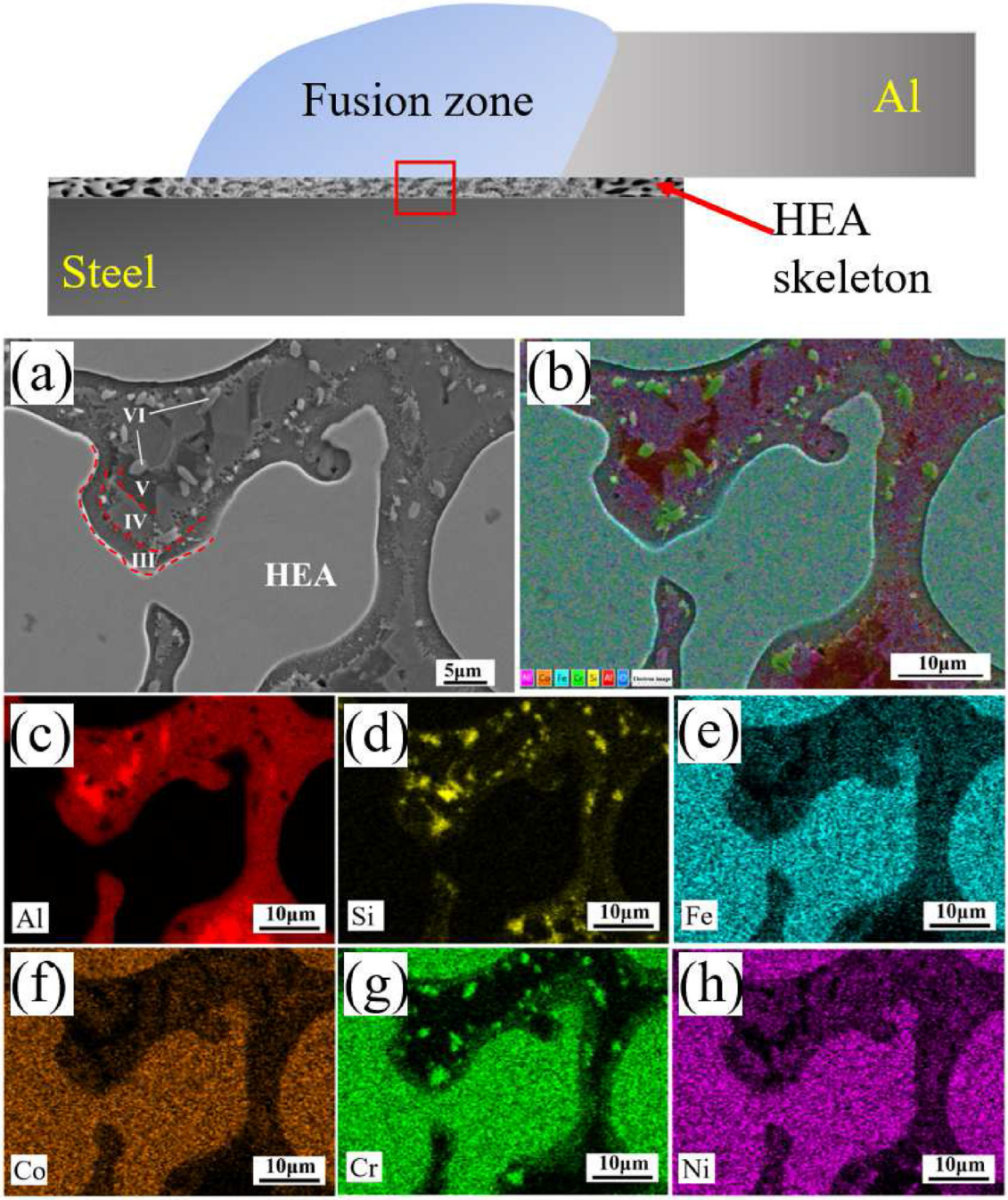

Fig. 5 – SEM image and EDS elemental mapping at the interface of laser Al/porous-coated steel joints.

speed of 0.3 m/min, defocus amount of +35 mm, and wire feed speed of 2 m/min.

After laser welding, samples for metallographic observations were mounted with epoxy resin, followed by standard grinding and polishing. The samples were then etched with Keller's reagent (95 mL H_2O+ 2.5 mL HNO_3+ 1.5 mL HCl+ 1.0 mL HF) for 6 s. The samples were analyzed using optical microscopy (OM, OLMPUS), scanning electron microscopy (SEM, ZEISS Gemini SEM 300), electron backscattered diffraction (EBSD, EDAX-TSL), and transmission electron microscopy (TEM, FEI Tecnai G2 F30) to analyze the microstructure and phase composition of the joint. The tensile test and fracture analysis of the laser joint were carried out by a tensile testing machine (MJDW-200B). The tensile-shear testing was evaluated at a cross-head speed of 1.0 mm/min at room temperature. The schematic diagram of the tensile test specimen is shown in Fig. 1(b). The microhardness measurements were conducted on a Vickers microhardness

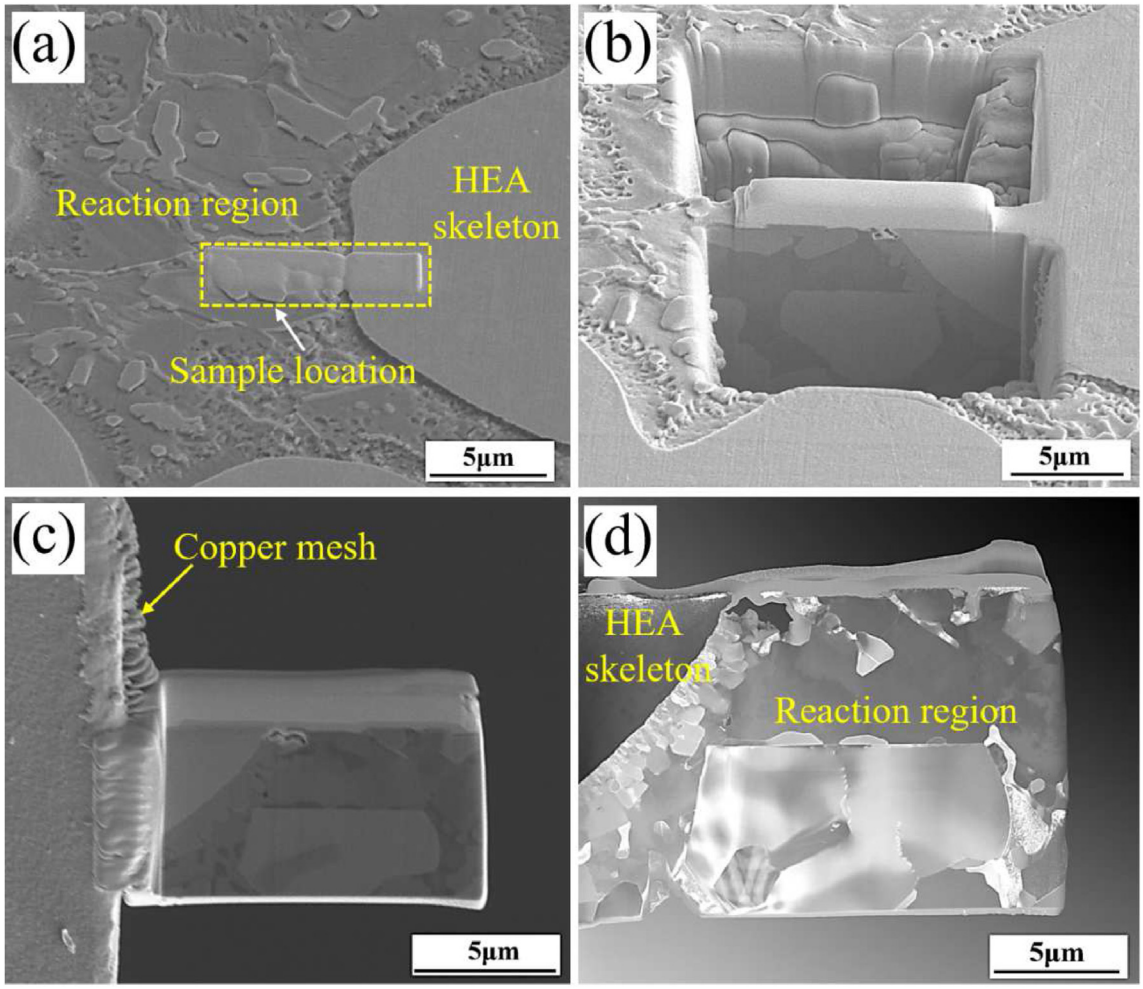

Fig. 6 – Preparing process for TEM sample of laser Al/steel joint with porous HEA coating: (a) region selected on origin metallographic sample, (b) ion milling on origin metallographic sample, (c) further ion milling on the sample attached on copper mesh, (d) finished TEM sample.

tester (HXD-1000TMS/LCD) with a load of 500 g and a dwelling time of 15 s.

3. Results and discussion

3.1. *Porous HEA coating*

Fig. 2(a) shows the top view appearance of the porous HEA coated steel, A homogenous coating without any macro-defects was observed. The size of the coating was 150 × 20 mm^2. Fig. 2(b–d) shows the SEM and EDS analysis of the cross-section of the porous HEA coating. As shown, the HEA particles formed an obvious sintering neck, and the pore size was randomly distributed, forming a three-dimensional interconnected open structure composed of HEA skeleton and open channels. The thickness, porosity, and average pore diameter were 275 μm, 44.63%, and 15.05 μm, respectively. In addition, the EDS analysis showed that Fe, Cr, Co, and Ni were homogeneously distributed on the coating with almost equal chemical composition. This equal atomic FeCrCoNi coating was composed of a single-phase FCC structure, as previously investigated [28]. The three-dimensional structure diagram of the coating was shown in Fig. 2(e).

3.2. *Interfacial microstructure*

Fig. 3(a and b) shows the weld appearances of laser Al/steel joints with the uncoated and porous coated steel substrates, respectively. Sound weld appearances were obtained both in uncoated and porous coated steel. Fig. 3(c and d) shows OM cross-sectional views of laser Al/steel joints with and without porous HEA coating. For the uncoated steel, it was observed that the fusion zone formed by the spreading of part of aluminum alloy base metal and Al–12Si alloy filler on the steel surface, and no obvious defects such as porosity were observed in the fusion zone. However, in the case of porous coated steel, the liquid filler metal was infiltrated into the porous coating skeleton. The contact angle and brazed width were measured to quantitatively compare the wettability of laser joints with uncoated steel to porous coated steel. The results showed that the contact angle decreased from 65.8° to

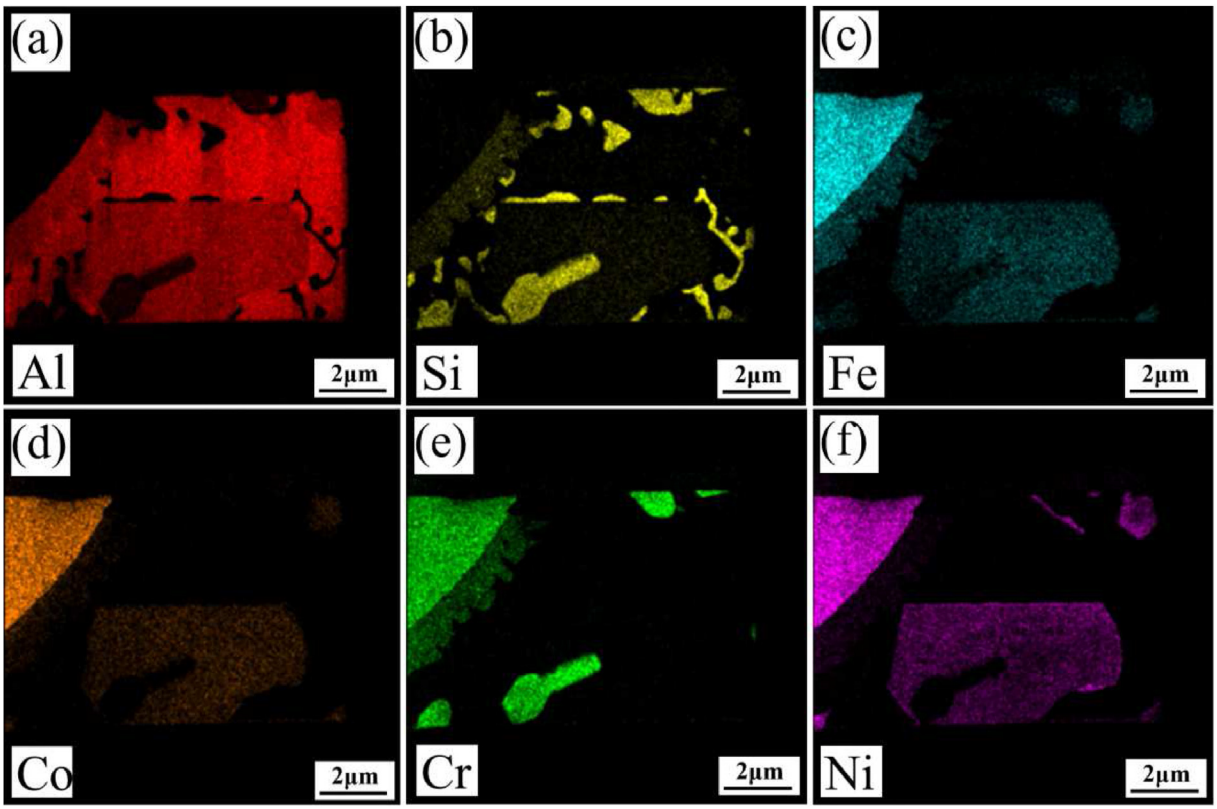

Fig. 7 – Element mapping in the TEM sample of laser Al/steel joint with porous HEA coating: (a) Al, (b) Si, (c) Fe, (d) Co, (e) Cr, (f) Ni.

56.7° and the brazing width increased from 5.1 mm to 5.9 mm from uncoated steel to porous coated steel. According to Tan et al. [29], A large brazing width with a small contact angle indicated a sound wettability of molten filler on the substrates. Therefore, the wettability and spreadability of laser Al/steel joints were improved by the porous HEA coating. Fig. 3(e and f) shows the SEM images of the interfacial region of the laser Al/steel joints with the uncoated and porous coated steel, respectively. For the uncoated steel, a gray layer of IMCs was observed at the interface between the fusion zone and steel. For the porous coated steel, the liquid alloy was infiltrated into the porous coating through the open structure under the capillary force forming a composite-like structure. This structure contained a HEA skeleton and a reaction region. In the reaction region, dark gray structures were generated wrapping the HEA skeleton. It apparently resulted from the metallurgical reaction between the coating and liquid from the fusion zone. Fig. 3(g) shows EDS elemental mapping in Fig. 3(f). Fe, Co, Cr, and Ni elements were dissolved into the liquid Al–12Si alloy forming the reaction region. EBSD analysis shows that the reaction products had very fine grain structure in the reaction region as shown in Fig. 3(h), which will be further characterized by SEM and TEM.

Fig. 4 shows the SEM images of the interfacial microstructure of laser Al/uncoated steel joints. As shown in Fig. 4(a), it was seen that two types (phases I and II) of laminal reaction layers were observed at the fusion zone/steel interface with a total thickness of 2 μm. Phase I adjacent to the fusion zone side, based on EDS results (Table 2), the composition of the continuous layered IMC was 67.39 at. % Al, 20.81 at. % Fe and 11.80 at. % Si, and the possible phase was identified as $Al_{7.2}Fe_{1.8}Si$. On the steel substrate side, the chemical composition of the layer was 65.23 at.% Al, 27.18 at.% Fe and 7.59 at.% Si (Table 2). It was speculated that the IMC was Fe(Al,Si)3. In fact, $Al_{7.2}Fe_{1.8}Si$ and Fe(Al,Si)3 phases were often observed in laser Al/steel joints [30,31]. To further analyze the distribution of elements at the interface, EDS element mapping was performed (Fig. 4(b–d)). It was obvious that Fe, Al, and Si elements enriched in the entire layered reaction layer, The results confirmed that Fe, Al, and Si elements were involved in inter-diffusion and interfacial reactions at the fusion zone/steel interface, thus promoting the formation of the IMCs.

Fig. 5 details the SEM and EDS mapping analysis at the interface of laser Al/porous-coated steel joints. Four regions, *i.e.*, III, IV, V, and VI, were divided according to their morphologies. A compact continuous layer was generated adjacent to the HEA skeleton (region III) with the composition shown in Table 2. The possible phase was a variant of the $Al_{7.2}Fe_{1.8}Si$ phase, namely a type of Al–Fe–Si-based ternary IMC, where Cr, Co, and Ni atoms shared some lattice sites with Fe atoms. In fact, the $Al_{7.2}Fe_{1.8}Si$ phase has a hexagonal crystal structure, which is often observed in laser Al/steel joints [30,31]. Attention must also be paid to Cr, which had an

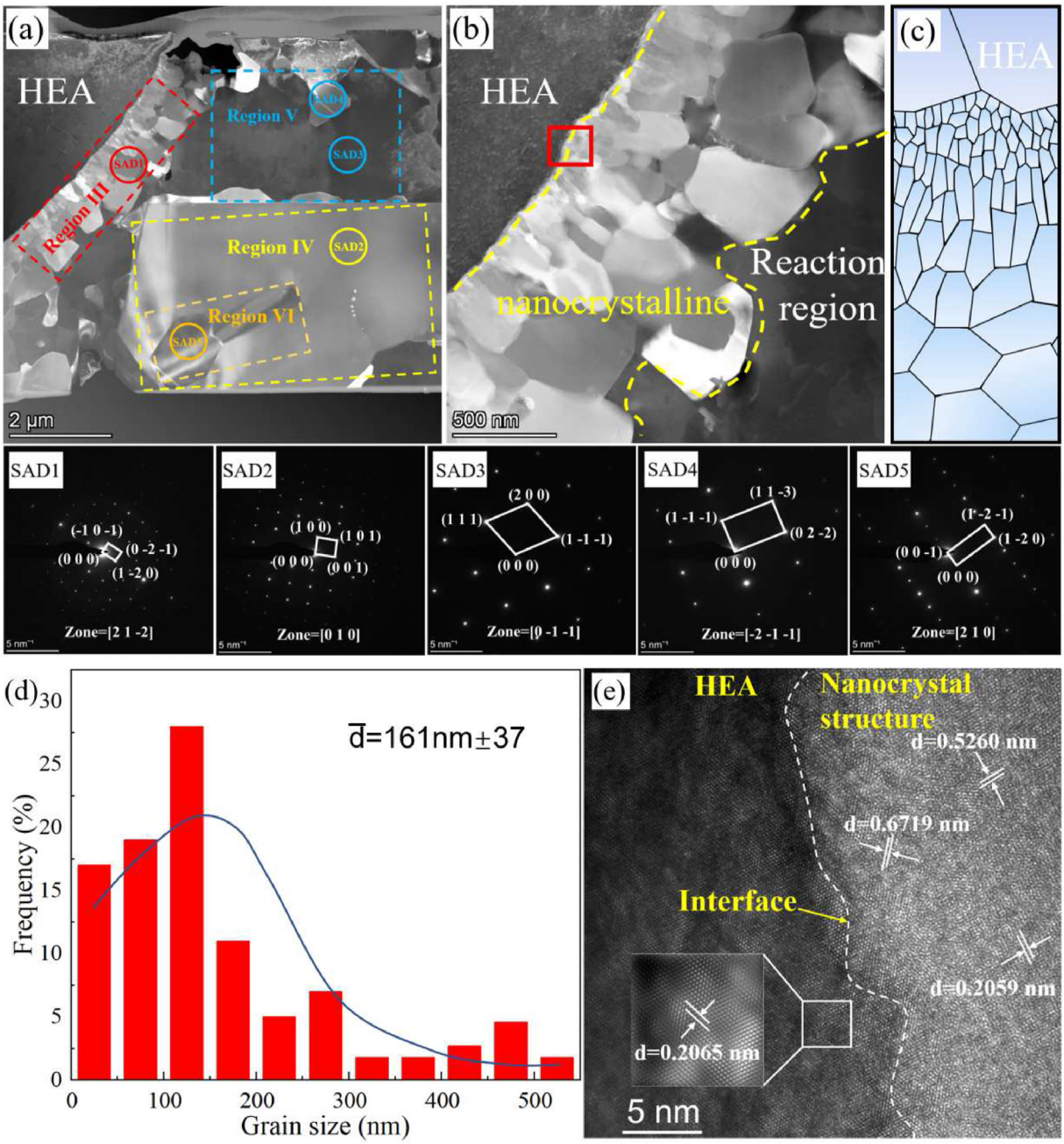

Fig. 8 – (a) Bright-field micrograph taken at the interface, with the circles indicating electron beam positions for obtaining diffraction patterns, (b) enlarged image of the interface of region III in (a), (c) schematically show the nanoscale gradient structure, (d) the statistical distribution of grain size of the gradient structured layer, (e) HR-TEM image of the red box in (b). The inset underneath (a–c) illustrated the SAPDs analysis of (a).

atomic ratio higher than that of Co, Ni, and Fe. This was because the diffusion coefficient of Cr in Al melt is the lowest, so Cr was enriched in region III [32]. Next to region III, a darker bulk structure was clearly observed (region IV). The composition of Al atoms increased to 77.78 at. % and the Ni content increased from 1.32 to 9.09 at.%. The negative mixing enthalpy of Al and Ni was reported to be very large, which led to a strong bond between Al and Ni. In opposition, the mixing enthalpy of Co, Cr, and Fe were similar and their bonding was relatively poor, thus promoting the formation of Al- and Ni-rich zones [33]. Hence, this region is likely to be composed of a variant of the Al_3Ni phase, which is a kind of Al–Ni-based binary IMC. From the EDS analysis, region V contained a type of Al-rich phase with a chemical content of 91.46 at.% Al, 7.29 at.% Si, with a trace amount of the remaining elements (Table 2). The lower atomic percentages of the elements Ni, Cr, Co, and Fe may be due to the sluggish diffusion effect of the HEA [34]. Hence, it is presumed that region V consists of the α-

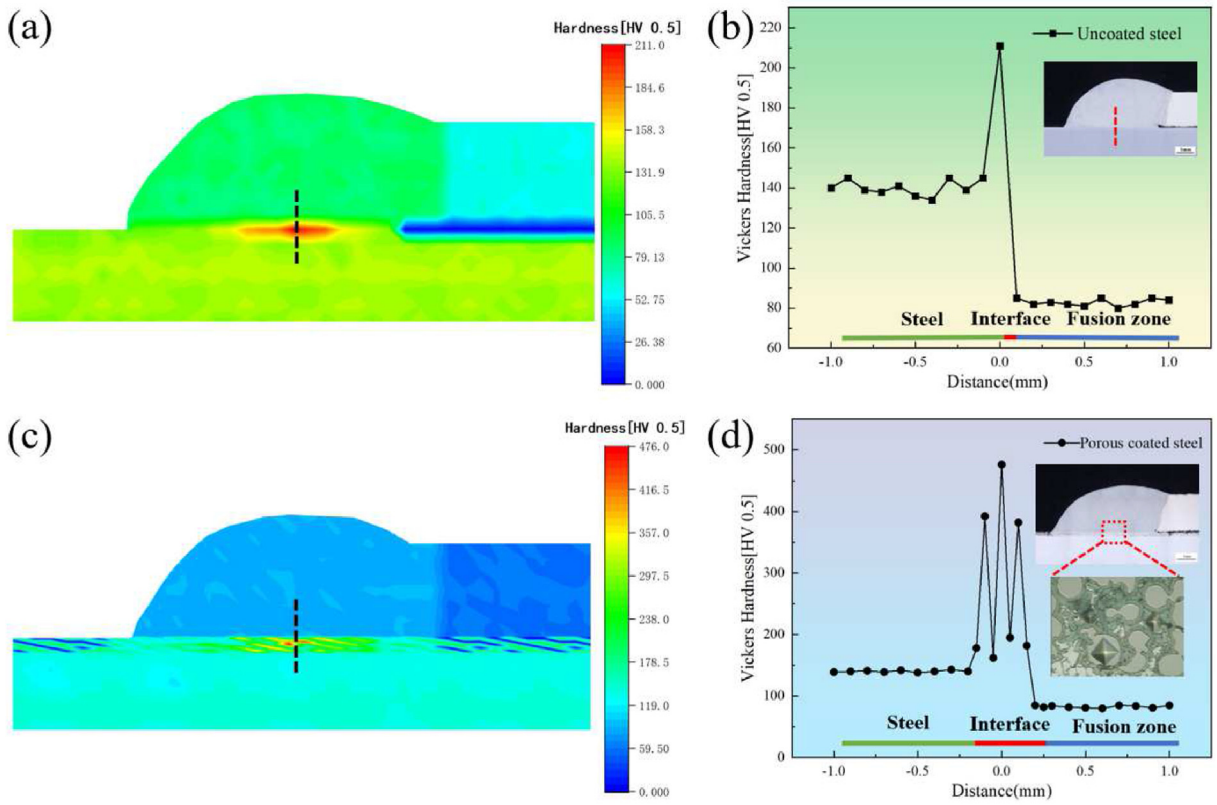

Fig. 9 – (a) Microhardness mapping across the laser joint with uncoated steel, (b) microhardness profiles obtained at the middle of the joint (black dashed line in (a)), (c) microhardness mapping across the laser joint with porous-coated steel, (d) microhardness profiles obtained at the middle of the joint (black dashed line in (c)).

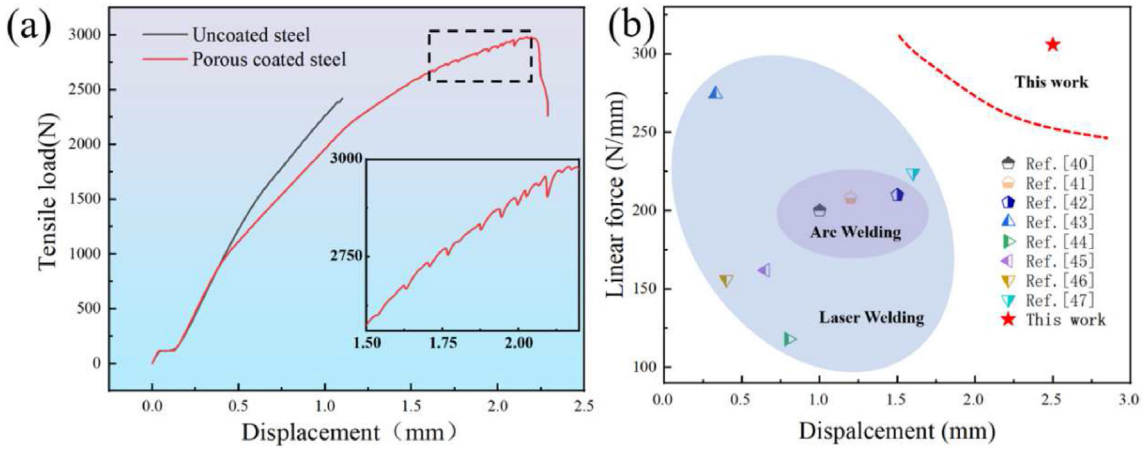

Fig. 10 – (a) Load-displacement curve of the uncoated steel and porous coated steel joints, (b) plot of tensile properties of dissimilar Al/steel joints obtained by various welding methods.

Al+β-Si eutectic phase. At region VI, some bright dispersoids were observed. From the EDS analysis (Table 2), the Cr: Si atomic ratio was close to 1:2. The possible phase was the $(Al,Si)_2Cr$ phase, where Al, Fe, Co, and Ni atoms shared some lattice sites with the Si atoms.

To further characterize the phase compositions shown in Fig. 5, TEM analysis was performed. The TEM sample was prepared using focus ion beam (FIB) technology, and the preparation process was shown in Fig. 6. Fig. 6(d) shows the selected region of the final produced TEM sample. Fig. 7 shows the element distributions in the FIB sample. It is obvious that the distribution of elements in the HEA skeleton is uniform, and the reaction zone has a eutectic structure rich in Al and Si, the massive phase rich in AlNi, and the dispersed particle structure rich in CrSi. This is consistent with the structure observed in the previous SEM analysis (Fig. 5).

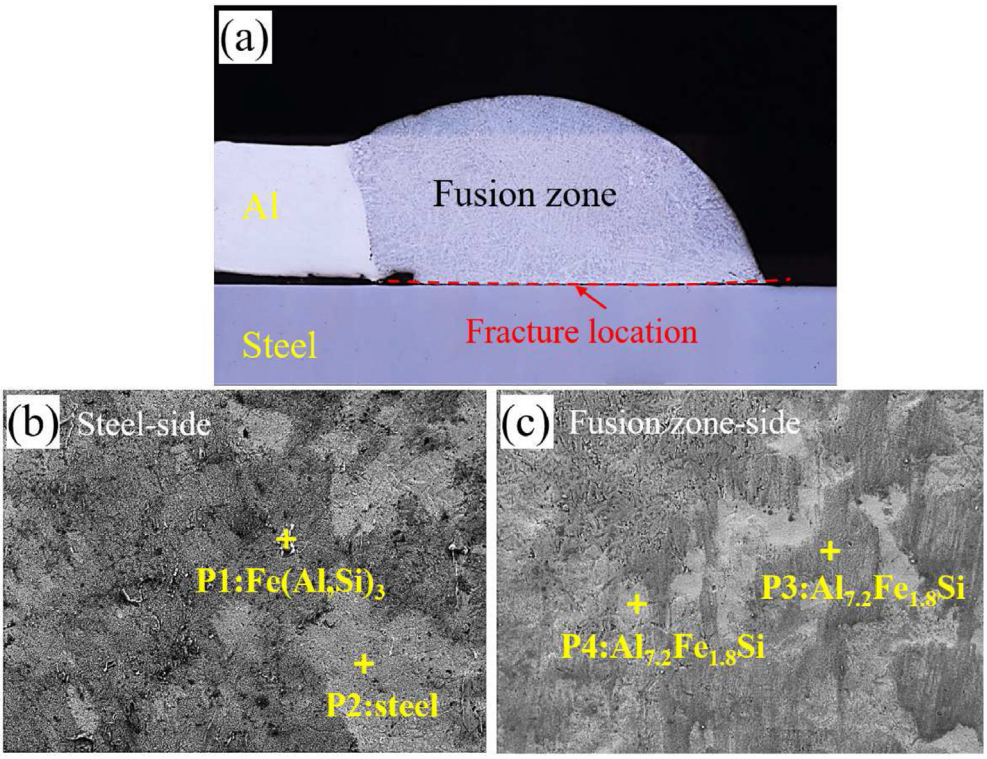

Fig. 11 – Fractographic analysis of laser Al/uncoated steel joints: (a) OM image of the fractured sample, (b) SEM images of the steel side, (c) SEM images of the fusion zone side.

Fig. 8(a) displays the high-angle annular bright field images of the TEM sample. It also showed four distinct regions: gradient nanoscale structures (Region III), bulk structure (Region IV), eutectic structure (Region V), and dispersoid particle structure (Region VI), which corresponded to the previous classification in Fig. 5. The selected area electron diffraction patterns (SADPs) were used to confirm the phase structure in the reaction region. The III-VI region SADPs represented the incident beams parallel to the axes of the [21–2] $_{Al7\cdot2Fe1\cdot8Si}$ (SAD1), [110] $_{Al3Ni}$ (SAD2), [0–1-1] $_{\alpha\text{-}Al}$ (SAD3), [–2–1-1] $_{\beta\text{-}Si}$ (SAD4), [210] $_{(Al,Si)2Cr}$ (SAD5) region, further confirmed the phases identified by SEM-EDS analyses. It is worth noting that a layer of nanoscale gradient structure was formed adjacent to the HEA sphere (refer to Fig. 8(b)). Fig. 8(c) shows the schematic diagram of the sectional nanoscale gradient microstructure of the interface region III. This gradient-structured layer was roughly 1 μm thick with an average grain size of 161 ± 37 nm (Fig. 8(d)). It was reported that nanograins were found to release the residual strains at the interface by restoring the misfit and plastic flow [35]. Besides, gradient structures are usually beneficial for the improvement of the yield strength because of a unique strain-hardening behavior generated where geometrically necessary dislocations (GNDs) are accumulated in the whole mechanical gradient layer to accommodate the strain gradients [36]. The mechanical testing used to probe the mechanical performance of the joints confirmed the statements above, as it will be detailed later. The formation mechanism of the nanoscale gradient structure was believed to be related to the sluggish diffusion effect of the HEA porous [37]. The sluggish diffusion effect is usually used to reveal the formation of nanoscale phases, as the nuclei are easier to form but grow slowly. In a previous investigation on the castability of a CuCoNiCrFe HEA, nano-precipitates with a size of 7–50 nm in diameter, close to the FCC phase in a spinodal plate, were formed [38]. Lattice fringes of the HEA were clearly seen in high resolution-TEM (HR-TEM) analysis, and

Table 3 – Chemical compositions of locations marked in Fig. 11 and 12 on the fracture surface (at. %).

Locations	Al	Si	Fe	Cr	Co	Ni	Possible phase
P1	64.87	7.57	27.56	–	–	–	$Fe(Al,Si)_3$
P2	1.43	0.21	98.36	–	–	–	Fe
P3	67.57	11.24	21.19	–	–	–	$Al_{7.2}Fe_{1.8}Si$
P4	71.54	11.61	16.85	–	–	–	$Al_{7.2}Fe_{1.8}Si$
P5	1.86	0.84	25.67	21.53	24.99	25.11	HEA
P6	76.12	1.61	5.65	1.77	3.57	11.28	Al_3Ni
P7	0.42	0.02	30.36	22.17	25.61	21.42	HEA
P8	84.31	6.20	3.39	2.10	2.05	1.95	α-Al+β-Si eutectic

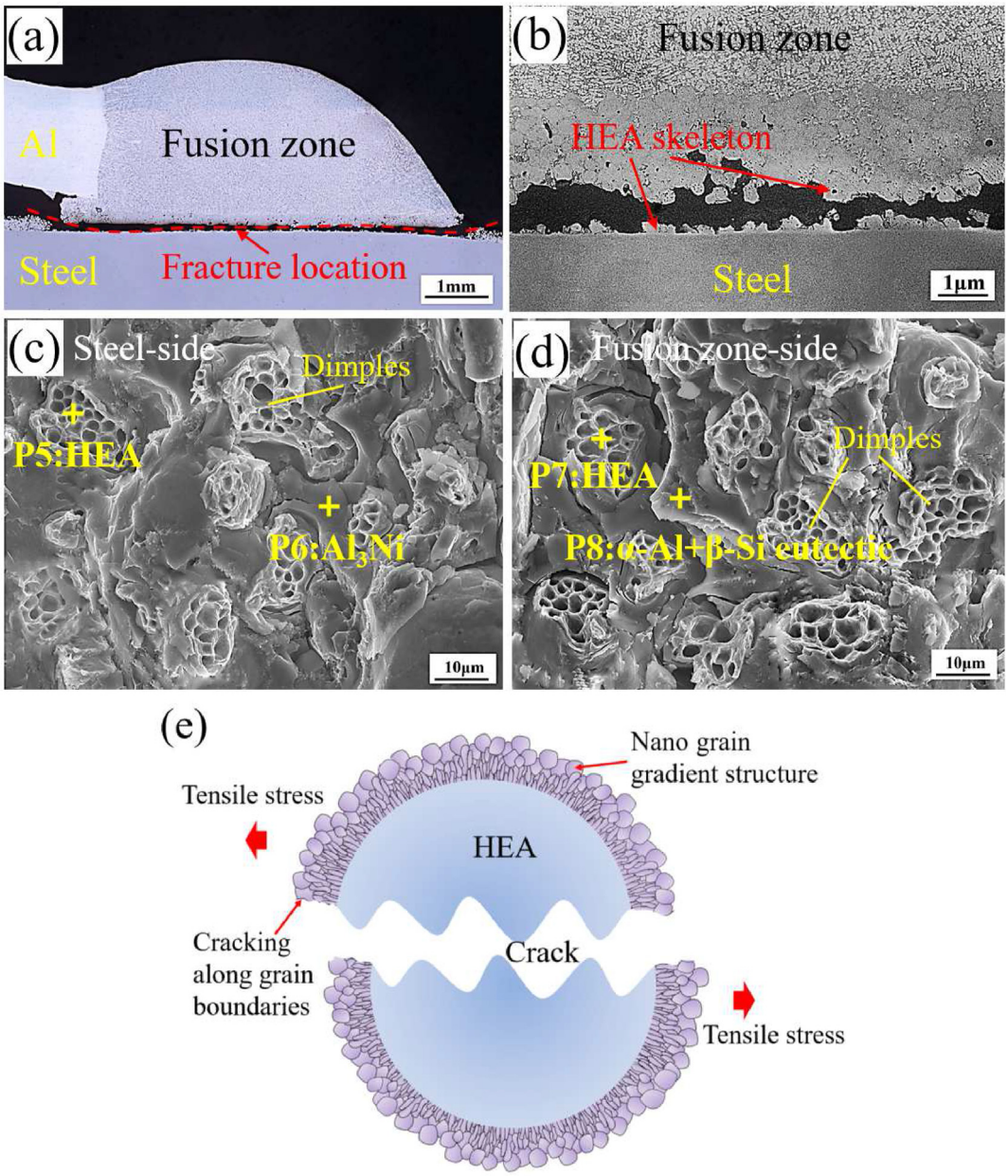

Fig. 12 – Fractographic analysis of laser Al/porous-coated steel joints: (a) OM image of the fractured sample, (b) enlarged cross-sectional view in (a), (c) SEM images of the steel side, (d) SEM images of the fusion zone side, (e) schematic diagram of the crack propagation path.

the nanograins were also observed near the interface in Fig. 8(e).

3.3. *Mechanical properties*

To further investigate the relationship between microstructure and local strength of the laser joints with uncoated and porous coated steel, microhardness mapping of the joints was carried out. Fig. 9 shows the two-dimensional microhardness map of the entire welded joint with uncoated and porous coated steel, showing the Vickers hardness of the steel, interface, and the fusion zone. The results showed that the hardness values of the steel, interface, and fusion zone varied greatly. The steel and fusion zone microhardness values were about 140 HV and 80 HV, respectively. For uncoated steel laser joints, the reaction layer microhardness increased sharply to 210.8 HV, which was far less than the microhardness of $Al_{7.2}Fe_{1.8}Si$ (956 HV) and $Fe(Al,Si)_3$ (883 HV) [39]. This was because the interfacial layer was too thin to be fully covered the micro indentation thus indicating an average microhardness at the interfacial region. However, for porous coated steel laser joints, it increased first and then decreased from the steel side to the fusion zone where the coating region showed the highest hardness~472 HV. It was worth noting that, unlike the sharp increase followed by a decrease at the uncoated steel interface, an alternative increasing and decrease of

hardness was observed at the interface which coincided with the characters of a composite-like structure. This kind of composite structure with soft structures composed of HEA skeleton and hard structures composed of $Al_{7.2}Fe_{1.8}Si$, Al_3Ni, and $(Al,Si)_2Cr$ was expected to be beneficial for the improvement of joint tensile properties [12].

Fig. 10(a) comparatively shows the tensile performance of the laser joints with and without the porous HEA coating. A maximum tensile load of 3059 N was obtained in the case of the coated steel, which was an improvement of 26.5% compared to the joint without coating (2418 N). The elongation was also increased by 101.8%, i.e., from, 1.12 mm without coating to 2.26 mm with coating. It was noteworthy that an obvious yielding process was seen in the load-displacement curve in the case of the joint with the coating, as shown in the inset in Fig. 10(a). It was mainly attributed to the strain hardening effect provided by the formation of the nanoscale gradient structure at the fusion zone/steel interface (refer to Fig. 8(b)). It was reported that gradient structures displayed an improved yield strength, and also exhibited optimized strength-ductility synergy and static toughness. This was due to the development of additional strengthening and strain hardening by hetero-deformation induced (HDI) due to the synergistic constraints between the gradient layers [36]. Conversely, an abrupt brittle fracture without any yielding was observed in the case of the uncoated steel. Fig. 10(b) displays the tensile properties of dissimilar Al/steel joints with various welding methods [40–47] and it is seen that the laser Al/steel joint in the present study displayed an outstanding linear force (fracture load per unit) and displacement when compared to other welded joints. It again confirmed the strengthening effect of the porous HEA coating.

3.4. *Fractography analysis*

Fig. 11 shows the fracture morphologies of the laser Al/uncoated steel joints. The laser joint failed at the fusion zone/steel interface (Fig. 11 a). Tearing edges and smoothly flat fracture planes were observed on the fracture interface, showing an obvious brittle fracture characteristic. Based on the EDS analysis, and the corresponding compositions of the marked points were shown in Table 3. At the steel side, the IMC at the fracture surface was identified as $Fe(Al,Si)_3$ (P1 in Fig. 11(b) and Table 3). The fracture surface at the fusion zone side exhibited very smooth characteristics, and $Al_{7.2}Fe_{1.8}Si$ was identified (P3 and P4 in Fig. 11(c) and Table 3). Therefore, it was inferred that the failure of the joint occurred within the IMCs layer.

Fig. 12 shows the fracture morphologies of the laser joint with the porous HEA-coated steel. It can be observed from Fig. 12 (a) that the laser joint fracture occurred near the coating. From the cross-sectional view of the fracture sample in Fig. 12(b), it was displayed that the fracture located at the lower part of the porous HEA coating adjacent to the steel substrate. A large number of dimples with various sizes and some cleavage steps were observed indicating that a mixture of plastic deformation and cleavage fracture was generated during the tensile process (Fig. 12 c-d). Based on the EDS analysis, Fe, Co, Cr, Ni elements at the dimples of the fracture were close to 1:1 (P5 and P7 in Fig. 12 c-d), so it was inferred that the dimple was an HEA skeleton (Table 3). Al_3Ni and α-Al+β-Si eutectic was observed at the cleavage steps fracture surface (P6 and P8 in Fig. 12 c-d). Thus, the porous coated steel laser joints fractured within the HEA skeleton and IMCs in the reaction zone. The schematic diagram for the crack propagation path further displayed the fracture location within the HEA skeleton (Fig. 12(e)). This suggested a robust bonding at the interface between the HEA sphere and nanoscale grain structure in the reaction region.

4. Conclusions

A FeCoCrNi porous HEA coating was prepared on the steel surface by vacuum sintering and then it was used as a transition layer for enhancing the laser Al/steel joints. The interface microstructure and mechanical performance of coated and uncoated laser Al/steel joints were comparatively investigated and the strengthening mechanism was discussed. The main conclusions were drawn as follows.

(1) The porous HEA coating improved the wettability and spreadability of the molten filler wire on the substrate. By using the porous HEA coating, the liquid alloy spread and infiltrated into the porous structure, the contact angle of the weld reduced from 65.8° to 56.7°, and the brazed width increased from 5.1 mm to 5.9 mm.
(2) For the uncoated steel, the interfacial microstructure consisted of laminated brittle $Al_{7.2}Fe_{1.8}Si$ and $Fe(Al,Si)_3$, while the reaction region in the case of porous coated steel changed to a composite-like structure containing a soft HEA skeleton and hard IMCs which was composed of $Al_{7.2}Fe_{1.8}Si$, Al_3Ni, and $(Al,Si)_2Cr$ phases.
(3) Because of the sluggish diffusion effect of HEAs, a layer of nanoscale gradient structure composed of $Al_{7.2}Fe_{1.8}Si$ was formed adjacent to the HEA skeleton, with the average grain size of 161 ± 37 nm. This kind of nanoscale gradient structure greatly enhanced bonding between the HEA sphere and reaction region by hetero-deformation induced extra strengthening and strain hardening, thus improving the joint tensile properties.
(4) By applying the porous HEA coating, the joint fracture load increased from 2418 N to 3059 N and the displacement increased from 1.12 mm to 2.26 mm.
(5) The fracture propagated through the HEA skeleton due to the strengthened HEA/reaction region interface, exhibiting a ductile fracture with the existence of various dimples.

CRediT authorship contribution statement

Min Zheng: Conceptualization, Data curation, Methodology, Software, Investigation, Writing – original draft. **Jin Yang:-** Conceptualization, Visualization, Validation, Funding acquisition, Writing – review & editing. **Jiayi Xu:**Data curation, Software, Investigation **Jiawei Jiang:** Data curation, Software, Investigation. **Hua Zhang:**Validation, Funding acquisition, Writing – review & editing, Supervision. **J.P. Oliveira:** Writing – review & editing, Supervision. **Xueqi Lv:** Formal analysis,

Writing – review & editing. **Jing Xue:**Resources, Writing – review & editing. **Zhuguo Li:**Supervision.

Declaration of competing interest

The authors declare that they have no known competing financial interests or personal relationships that could have appeared to influence the work reported in this paper.

Acknowledgments

This work was supported by the National Natural Science Foundation of China (No. 52275155) and Class III Peak Discipline of Shanghai—Materials Science and Engineering. JPO acknowledges funding by national funds from FCT - Fundação para a Ciência e a Tecnologia, I.P., in the scope of the projects LA/P/0037/2020, UIDP/50025/2020 and UIDB/50025/2020 of the Associate Laboratory Institute of Nanostructures, Nanomodelling and Nanofabrication – i3N.

REFERENCES

[1] Lei Z, Liu X, Wu Y, Wang H, Jiang S, Wang S, Hui X, Wu Y, Gault B, Kontis P. Enhanced strength and ductility in a high-entropy alloy via ordered oxygen complexes. Nature 2018;563:546–50. https://doi.org/10.1038/s41586-018-0685-y.

[2] Rao Z, Tung P, Xie R, Wei Y, Zhang H, Ferrari A, Klaver T, Körmann F, Sukumar PT, da Silva AK. Machine learning-enabled high-entropy alloy discovery. Mater Sci 2022;2202:13753. https://doi.org/10.48550/arXiv.2202.13753.

[3] Lin C, Shiue R-K, Wu S-K, Lin Y-S. Dissimilar infrared brazing of CoCrFe (Mn) Ni equiatomic high entropy alloys and 316 stainless steel. Crystals 2019;9:518. https://doi.org/10.3390/cryst9100518.

[4] Shaysultanov D, Stepanov N, Malopheyev S, Vysotskiy I, Sanin V, Mironov S, Kaibyshev R, Salishchev G, Zherebtsov S. Friction stir welding of a carbon-doped CoCrFeNiMn high-entropy alloy. Mater Char 2018;145:353–61. https://doi.org/10.1016/j.matchar.2018.08.063.

[5] Lei Y, Hu S, Yang T, Song X, Luo Y, Wang G. Vacuum diffusion bonding of high-entropy Al0. 85CoCrFeNi alloy to TiAl intermetallic. J Mater Process Technol 2020;278:116455. https://doi.org/10.1016/j.jmatprotec.2019.116455.

[6] Shen J, Gonçalves R, Choi YT, Lopes J, Yang J, Schell N, Kim HS, Oliveira J. Microstructure and mechanical properties of gas metal arc welded CoCrFeMnNi joints using a 410 stainless steel filler metal. Mater. Sci. Eng. A 2022;857:144025. https://doi.org/10.1016/j.msea.2022.144025.

[7] Shen J, Gonçalves R, Choi YT, Lopes J, Yang J, Schell N, Kim HS, Oliveira J. Microstructure and mechanical properties of gas metal arc welded CoCrFeMnNi joints using a 308 stainless steel filler metal. Scripta Mater 2023;222:115053. https://doi.org/10.1016/j.scriptamat.2022.115053.

[8] Fiocchi J, Casati R, Tuissi A, Biffi CA. Laser beam welding of CoCuFeMnNi high entropy alloy: processing, microstructure, and mechanical properties. Adv Eng Mater 2022;24:2200523. https://doi.org/10.1002/adem.202200523.

[9] Yin Q, Chen G, Ma Y, Zhang B, Huang Y, Dong Z, Cao J. Strengthening mechanism for high-entropic weld of molybdenum/Kovar alloy electron beam welded joint. Mater. Sci. Eng. A 2022;851:143619. https://doi.org/10.1016/j.msea.2022.143619.

[10] Lopes JG, Oliveira JP. A short review on welding and joining of high entropy alloys. Metals-Basel 2020;10:212. https://doi.org/10.3390/met10020212.

[11] Zhang L, Shi J, Li H, Tian X, Feng J. Interfacial microstructure and mechanical properties of ZrB2SiCC ceramic and GH99 superalloy joints brazed with a Ti-modified FeCoNiCrCu high-entropy alloy. Mater Des 2016;97:230–8. https://doi.org/10.1016/j.matdes.2016.02.055.

[12] Wang G, Yang Y, Wang M, He R, Tan C, Cao W, Xu H. Brazing ZrB2-SiC ceramics to Nb with a novel CoFeNiCrCu high entropy alloy. J Eur Ceram Soc 2021;41:54–61. https://doi.org/10.1016/j.jeurceramsoc.2020.08.050.

[13] Azhari-Saray H, Sarkari-Khorrami M, Nademi-Babahadi A, Kashani-Bozorg SF. Dissimilar resistance spot welding of 6061-T6 aluminum alloy/St-12 carbon steel using a high entropy alloy interlayer. Intermetallics 2020;124:106876. https://doi.org/10.1016/j.intermet.2020.106876.

[14] Shirzadi A, Zhu Y, Bhadeshia H. Joining ceramics to metals using metallic foam. Mater. Sci. Eng. A 2008;496:501–6. https://doi.org/10.1016/j.msea.2008.06.007.

[15] Wang Z, Wang G, Li M, Lin J, Ma Q, Zhang A, Zhong Z, Qi J, Feng J. Three-dimensional graphene-reinforced Cu foam interlayer for brazing C/C composites and Nb. Carbon 2017;118:723–30. https://doi.org/10.1016/j.carbon.2017.03.099.

[16] Sun R, Zhu Y, Guo W, Peng P, Li L, Zhang Y, Fu J, Li F, Zhang L. Microstructural evolution and thermal stress relaxation of Al2O3/1Cr18Ni9Ti brazed joints with nickel foam. Vacuum 2018;148:18–26. https://doi.org/10.1016/j.vacuum.2017.10.030.

[17] Xu W, Li H, Yang J, Zhao Y, Oliveira J, Liu H, Zhang Z, Tan C. Dynamic wetting and spreading mechanisms regulated by elemental Ni in a Mg/steel immiscible system during laser processing. J Manuf Process 2022;80:600–11. https://doi.org/10.1016/j.jmapro.2022.06.042.

[18] Xue J, Guo W, Yang J, Xia M, Zhao G, Tan C, Wan Z, Chi J, Zhang H. In-situ observation of microcrack initiation and damage nucleation modes on the HAZ of laser-welded DP1180 joint. J Mater Sci Technol 2023. https://doi.org/10.1016/j.jmst.2023.01.001.

[19] Bridges D, Zhang S, Lang S, Gao M, Yu Z, Feng Z, Hu A. Laser brazing of a nickel-based superalloy using a Ni-Mn-Fe-Co-Cu high entropy alloy filler metal. Mater Lett 2018;215:11–4. https://doi.org/10.1016/j.matlet.2017.12.003.

[20] Liu D, Wang J, Xu M, Jiao H, Tang Y, Li D, Zhao L, Han S. Evaluation of dissimilar metal joining of aluminum alloy to stainless steel using the filler metals with a high-entropy design. J Manuf Process 2020;58:500–9. https://doi.org/10.1016/j.jmapro.2020.08.031.

[21] Li T, Xu J, Bi X, Li R. Microstructure evolution and crack propagation mechanism during laser lap welding of Ti6Al4V and DP780 steel with CoCrNi powder. Mater Des 2022;223:111126. https://doi.org/10.1016/j.matdes.2022.111126.

[22] Ogura T, Wakazono R, Yamashita S, Saida K. Dissimilar laser brazing of aluminum alloy and galvannealed steel and defect control using interlayer. Weld World 2020;64:697–706. https://doi.org/10.1007/s40194-020-00858-7.

[23] Tao T, Liu J, Zhou D, Li H. Influence of laser-Sn powder coupling on microstructure and mechanical properties of fusion welded AZ31B-alloy to DP590-steel. Opt Laser Technol 2022;152:108091. https://doi.org/10.1016/j.optlastec.2022.108091.

[24] Wu M, Luo Z, Li Y, Liu L, Ao S. Effect of heat source parameters on weld formation and defects of oscillating laser-TIG hybrid welding in horizontal position. J Manuf

Process 2022;83:512–21. https://doi.org/10.1016/j.jmapro.2022.09.030.
[25] Xia H, Li L, Tan C, Yang J, Li H, Song W, Zhang K, Wang Q, Ma N. In situ SEM study on tensile fractured behavior of Al/steel laser welding-brazing interface. Mater Des 2022;224:111320. https://doi.org/10.1016/j.matdes.2022.111320.
[26] Yang J, Su J, Yu Z, Zhang G, Lin S, Li Y, Zhou N. Influence of Ni interlayer width on interfacial reactions and mechanical properties in laser welding/brazing of Al/Mg lap joint. Sci Technol Weld Join 2020;25:37–44. https://doi.org/10.1080/13621718.2019.1607487.
[27] Yang J, Yu Z, Li Y, Zhang H, Zhou N. Laser welding/brazing of 5182 aluminium alloy to ZEK100 magnesium alloy using a nickel interlayer. Sci Technol Weld Join 2018;23:543–50. https://doi.org/10.1080/13621718.2018.1425182.
[28] Zheng M, Zhang H, Gao Y, Zhao Y, Tan C, Song X, Yang J. Influence of porous high entropy alloy coating on wetting behavior and interfacial microstructure of Al-Si alloy on steel substrate. J Alloys Compd 2022;912:165154. https://doi.org/10.1016/j.jallcom.2022.165154.
[29] Tan C, Chen B, Meng S, Zhang K, Song X, Zhou L, Feng J. Microstructure and mechanical properties of laser welded-brazed Mg/Ti joints with AZ91 Mg based filler. Mater Des 2016;99:127–34. https://doi.org/10.1016/j.matdes.2016.03.073.
[30] Yang J, Oliveira J, Li Y, Tan C, Gao C, Zhao Y, Yu Z. Laser techniques for dissimilar joining of aluminum alloys to steels: a critical review. J Mater Process Technol 2022;301:117443. https://doi.org/10.1016/j.jmatprotec.2021.117443.
[31] Yang J, Su J, Gao C, Zhao Y, Liu H, Pedro OJ, Tan C, Yu Z. Effect of heat input on interfacial microstructure, tensile and bending properties of dissimilar Al/steel lap joints by laser Welding-brazing. Opt Laser Technol 2021;142:107218. https://doi.org/10.1016/j.optlastec.2021.107218.
[32] Tang S, Luo Y, Zhang G, Liu Y. Interface structure and formation mechanism of FeCrCoNiMn high entroy alloy hot-dipping in molten aluminum. Mater. Rep. 2016;30:76–80. https://doi.org/10.11896/j.issn.1005-023X.2016.20.017.
[33] Lu Y, Jiang H, Guo S, Wang T, Cao Z, Li T. A new strategy to design eutectic high-entropy alloys using mixing enthalpy. Intermetallics 2017;91:124–8. https://doi.org/10.1016/j.intermet.2017.09.001.
[34] Yeh J-W. Recent progress in high entropy alloys. Eur J Control 2006;31:633–48. https://doi.org/10.3166/acsm.31.633-648.
[35] Spaepen F. Interfaces and stresses in thin films. Acta Mater 2000;48:31–42. https://doi.org/10.1016/S1359-6454(99)00286-4.
[36] Guo F, Wang Y, Wang M, He Q, Ran H, Huang C, Zhu Y. Hetero-deformation induced strengthening and toughening of pure iron with inverse and multi-gradient structures. Mater. Sci. Eng. A 2020;782:139256. https://doi.org/10.1016/j.msea.2020.139256.
[37] Zhang Y, Zuo TT, Tang Z, Gao MC, Dahmen KA, Liaw PK, Lu ZP. Microstructures and properties of high-entropy alloys. Prog Mater Sci 2014;61:1–93. https://doi.org/10.1016/j.pmatsci.2013.10.001.
[38] Yeh JW, Chen SK, Lin SJ, Gan JY, Chin TS, Shun TT, Tsau CH, Chang SY. Nanostructured high-entropy alloys with multiple principal elements: novel alloy design concepts and outcomes. Adv Eng Mater 2004;6:299–303. https://doi.org/10.1002/adem.200300567.
[39] Yang J, Yu Z, Li Y, Zhang H, Guo W, Zhou N. Influence of alloy elements on microstructure and mechanical properties of Al/steel dissimilar joint by laser welding/brazing. Weld World 2018;62:427–33. https://doi.org/10.1007/s40194-017-0540-z.
[40] Pouranvari M, Abbasi M. Dissimilar gas tungsten arc weld-brazing of Al/steel using Al-Si filler metal: microstructure and strengthening mechanisms. J Alloys Compd 2018;749:121–7. https://doi.org/10.1016/j.jallcom.2018.03.224.
[41] Cao R, Yu G, Chen J, Wang P-C. Cold metal transfer joining aluminum alloys-to-galvanized mild steel. J Mater Process Technol 2013;213:1753–63. https://doi.org/10.1016/j.jmatprotec.2013.04.004.
[42] Mezrag B, Deschaux-Beaume F, Sabatier L, Wattrisse B, Benachour M. Microstructure and properties of steel-aluminum cold metal transfer joints. J Mater Process Technol 2020;277:116414. https://doi.org/10.1016/j.jmatprotec.2019.116414.
[43] Li L, Xia H, Tan C, Ma N. Effect of groove shape on laser welding-brazing Al to steel. J Mater Process Technol 2018;252:573–81. https://doi.org/10.1016/j.jmatprotec.2017.10.025.
[44] Mukherjee M, Kundu J, Shome M. Effect of processing parameters on the interface characteristics and joint strengths of aluminium-on-steel lap joints produced using conduction mode laser welding. Weld World 2022;66:2461–82. https://doi.org/10.1007/s40194-022-01392-4.
[45] Hu Y, Zhang Y, Mi G, Wang C, Zhang W, Zhang X. Effects of Si contents in filling wires on microstructure evolution and properties of Al-steel dissimilar joint by laser welding-brazing. J Mater Res Technol 2021;15:1896–904. https://doi.org/10.1016/j.jmrt.2021.09.053.
[46] Yuan R, Deng S, Cui H, Chen Y, Lu F. Interface characterization and mechanical properties of dual beam laser welding-brazing Al/steel dissimilar metals. J Manuf Process 2019;40:37–45. https://doi.org/10.1016/j.jmapro.2019.03.005.
[47] Javadinejad HR, Lee M, Shim CH, Chang HJ, Kim JH. Interfacial reaction mechanism during laser brazing of Zn–Mg–Al-coated steel to AA 6061 aluminum alloy. J Manuf Process 2022;83:471–87. https://doi.org/10.1016/j.jmapro.2022.09.013.